2019

A Coupled Wicking and Evaporation Model for Prediction of Pool Boiling Critical Heat Flux on Structured Surfaces

H. Hu
Purdue University

J. A. Weibel
Purdue University, jaweibel@purdue.edu

S V. Garimella
Purdue University, sureshg@purdue.edu

Hu, H.; Weibel, J. A.; and Garimella, S V., "A Coupled Wicking and Evaporation Model for Prediction of Pool Boiling Critical Heat Flux on Structured Surfaces" (2019). *CTRC Research Publications.* Paper 339.
http://dx.doi.org/https://doi.org/10.1016/j.ijheatmasstransfer.2019.03.005

A Coupled Wicking and Evaporation Model for Prediction of Pool Boiling Critical Heat Flux on Structured Surfaces

Han Hu, Justin A. Weibel[1], and Suresh V. Garimella[1]
School of Mechanical Engineering, Cooling Technologies Research Center
Purdue University, 585 Purdue Mall, West Lafayette, IN 47907 USA

ABSTRACT. Boiling is an effective heat transfer mechanism that is central to a variety of industrial processes including electronic systems, power plants, and nuclear reactors. Micro-/nano-structured surfaces have been demonstrated to significantly enhance the critical heat flux (CHF) during pool boiling, but there is no consensus on how to predict the structure-induced CHF enhancement. In this study, we develop an analytical model that takes into consideration key mechanisms that govern CHF during pool boiling on structured surfaces, namely, capillary wicking and evaporation of the liquid layer underneath the bubble. The model extends existing wicking-based CHF theories by introducing the competing evaporation mechanism. The model reveals a wicking-limited regime where CHF increases monotonically with the wicking flux, and an evaporation-limited regime where additional increases in the wicking flux do not significantly affect CHF. The model predictions are shown to agree with experimental CHF data from the literature for boiling of water on surfaces structured with square micropillar arrays. A parametric study is performed for such micropillared surfaces and has identified the optimal structure based on the competition between wicking and evaporation, capillary pressure and viscous resistance, and conduction and liquid-vapor interfacial resistance.

Keywords: pool boiling, critical heat flux, structured surfaces, wicking, evaporation

[1] Corresponding author. E-mail: jaweibel@purdue.edu (J.A. Weibel), sureshg@purdue.edu (S.V. Garimella)

Nomenclature

D	pillar diameter, m
d_{b}	bubble departure diameter, m
d_{dry}	dry spot diameter, m
d_{dry}^{*}	critical dry spot diameter, m
g	gravitational acceleration, $\mathrm{m^2/s}$
H	pillar height, m
h_{fg}	enthalpy of vaporization, J/kg
h_{lv}	evaporation heat transfer coefficient, $\mathrm{W/(m^2 \cdot K)}$
K	permeability of structures, $\mathrm{m^2}$
K_{B}	effective permeability, $\mathrm{m^2}$
k_{l}	thermal conductivity, $\mathrm{W/(m \cdot K)}$
M	molar mass, kg/mol
P	pillar pitch, m
P_0	bulk liquid pressure, Pa
P_{C}	capillary pressure, Pa
P_{l}	liquid pressure, Pa
P_{v}	vapor pressure, Pa
q''_{CHF}	critical heat flux, $\mathrm{W/m^2}$
q''_{e}	evaporation heat flux, $\mathrm{W/m^2}$
$q''_{\mathrm{CHF,f}}$	critical heat flux on flat surfaces, $\mathrm{W/m^2}$
$q''_{\mathrm{CHF,s}}$	Structure-induced CHF enhancement, $\mathrm{W/m^2}$
q''_{w}	wicking heat flux, $\mathrm{W/m^2}$
r	radial coordinate
r_{area}	correction factor for wetted area
r_{s}	roughness ratio of the side wall
R	wicking front location, m
R^{*}	radius of curvature, m

Greek letters

α_{fit}	fitting parameter
$\Delta\rho_{\mathrm{lv}}$	difference in liquid and vapor density, $\mathrm{kg/m^3}$
δ	liquid film thickness, m
δ_{c}	critical film thickness, m
ε	porosity
θ_{equ}	equilibrium contact angle at room temperature, °
$\theta_{\mathrm{equ,b}}$	equilibrium contact angle at boiling point, °
$\theta_{\mathrm{rec,b}}$	receding contact angle at boiling point, °
λ_{RT}	critical wavelength of Rayleigh-Taylor instability, m
μ	dynamic viscosity, $\mathrm{m^2/s}$
ρ_{l}	liquid density, $\mathrm{kg/m^3}$
ρ_{s}	solid density, $\mathrm{kg/m^3}$
ρ_{v}	vapor density, $\mathrm{kg/m^3}$
σ_{lv}	surface tension, $\mathrm{J/m^2}$
$\hat{\sigma}$	accommodation coefficient
τ	stress, Pa
Φ_{e}	evaporation rate, $\mathrm{m^3/s}$
Φ_{g}	gravity-driven flow rate, $\mathrm{m^3/s}$
Φ_{w}	wicking rate, $\mathrm{m^3/s}$
$\Phi_{\mathrm{w,ch}}$	characteristic wicking rate, $\mathrm{m^3/s}$
ϕ''_{e}	evaporation flux, m/s
$\phi''_{\mathrm{e,avg}}$	average evaporation flux from the meniscus, m/s
$\phi''_{\mathrm{e,ch}}$	characteristic evaporation flux, m/s
ϕ''_{w}	wicking flux, m/s
$\phi''_{\mathrm{w,ch}}$	characteristic wicking flux, m/s
ω	superhydrophilicity metric $\omega = P_{\mathrm{C}} K H$, $\mathrm{Pa \cdot m^3}$

R_u	universal gas constant, J/(mol·K)	ω^*	modified superhydrophilicity metric $\omega = P_C K_B H$, Pa·m^3
T_{boil}	liquid boiling point, K	*Subscripts*	
T_s	surface temperature, K	ch	characteristic quantities
T_v	vapor temperature, K	e	evaporation
u_r	radial flow velocity, m/s	w	wicking

1. Introduction

Boiling is a key industrial transport process central to the operation of power plants, nuclear reactors, electronic systems, and other applications. While nucleate boiling offers the potential for high heat dissipation efficiency by taking advantage of the latent heat of vaporization, there exists a critical heat flux (CHF) limit above which an insulating vapor layer covers the heated surface. Above CHF, the heat dissipation efficiency is reduced by orders of magnitude compared to nucleate boiling. Therefore, it is of vital importance to accurately predict CHF to inform the design of surfaces that extend this limit.

Over a half-century ago, Zuber [1] derived a hydrodynamics-based model that accurately captures the pool boiling CHF on flat surfaces [2-4]. Recent experimental studies [2, 3, 5-18] have shown that using micro-/nano-structured surfaces can enhance CHF well above Zuber's limit. A variety of mechanisms have been proposed to explain the structure-induced CHF enhancement, including increased three-phase contact line length [11, 16], microconvection around the bubble [19], increased departure frequency of coalesced bubbles [3], and liquid rewetting via capillary wicking [2, 3, 5, 7, 8, 11, 13, 14]. Among these mechanisms, capillary wicking has been the most widely agreed upon, with strong support from experimental data [2, 5, 10, 17]. A number of CHF models have been developed [2, 8, 10, 17, 20, 21] based on this wicking mechanism, sharing a common formulation of $q''_{CHF} = q''_{CHF,f} + q''_w$, where $q''_{CHF,f}$ represents the critical heat flux predicted for a flat surface (*i.e.,* without the capillary wicking) and q''_w represents the amount of CHF enhancement induced by capillary wicking. While $q''_{CHF,f}$ is usually calculated with established CHF models based on hydrodynamics [1], the balance of forces acting on bubbles [22], or gravity-driven rewetting [8, 10], there is no consensus on how the wicking-induced CHF enhancement q''_w should be predicted.

Table 1 summarizes the empirical, analytical, and semi-analytical models available to predict CHF on structured surfaces. All symbols are defined in the source references, except that a generic symbol (α_{fit}) is used to represent the fitting parameters in the empirical and semi-analytical models. Many wicking-based CHF models rely on empirical relations that are developed by correlating CHF with experimentally-measured wicking properties [2, 17, 20]. Ahn *et al.* [17] characterized the wicking capability of structured surfaces by measuring the volume flux of a droplet wicked into a structured surface, and assumed that CHF increased monotonically with the measured wicked volume flux. Their results demonstrated wicking to be a key mechanism for CHF enhancement on structured surfaces. Rahman *et al.* [2] adopted the same method as Ahn *et al.* [17] to characterize the wicking capability of a broader range of structured surfaces, including biotemplated nanostructures, square micropillar arrays of different diameter, height, and pitch, and hierarchical structures. Their experimental data strongly supported a linear relationship between the CHF and the measured wicked volume flux. Kim *et al.* [20] measured the wicking distance of droplets spreading on structured surfaces and fitted the wicking distance as a square-root function of time. A wicking factor was defined using the coefficient of the fitted relationship, and CHF was reported to scale linearly with the wicking factor. Despite good agreement with experimental data, these correlations strongly depend on the experimentally measured wicking properties, limiting their applicability to the design of surfaces for enhanced CHF.

Recently, efforts have been made to develop analytical and semi-analytical models (including fitted parameters) to predict the wicking-induced CHF enhancement [8, 10, 21]. Dhillon *et al.* [10] derived an analytical model for CHF based on rewetting of a dry spot on the boiling surface and predicted an optimal structure spacing resulting from the competition between capillary pressure and viscous resistance. Kim *et al.* [8] derived a model for CHF on structured surfaces assuming that CHF was governed by liquid-supply capability from the gravitational and microscopic pressure potentials including capillary and disjoining pressures. Li and Huang [21] used Kandlikar's model [22] for $q''_{\text{CHF,f}}$ and derived the wicking-induced enhancement q''_{w} as a linear function of the wicking front velocity in the surface structures. Their model was semi-analytical, with the coefficient of the linear relationship fitted using experimental data. We note that existing wicking-based CHF models have focused on developing wicking parameters to characterize the wicking behavior of liquid on structured surfaces, followed by the formulation of a relationship between CHF enhancement and the wicking parameters developed. A variety of standalone

wicking parameters have been proposed, among which Xiao *et al.* [23] and Allred *et al.* [24] have defined representative parameters for linear wicking and radial wicking, respectively. Xiao *et al.* [23] reported that the volumetric rate of linear wicking follows the Washburn-type square-root law; a propagation coefficient was introduced for the square-root relationship. Allred *et al.* [24] analyzed the volumetric rate of radial wicking and introduced a superhydrophilicity metric defined as the product of capillary pressure, flow permeability, and the height of the structure to characterize radial wicking behavior. Although these two studies [23, 24] did not propose CHF theories, the wicking parameters introduced can be useful for modeling CHF enhancement during pool boiling.

Table 1. Summary of empirical, semi-analytical, and analytical wicking-based CHF models and proposed wicking parameters.

Reference	CHF Model	Type	Wicking Parameter
Ahn *et al.* [17]	$q''_{CHF} = \alpha_{fit,1} q''_{Kandlikar} + \alpha_{fit,2}\, \rho_l h_{fg} \Phi_w / A_h$ *	Empirical	Volumetric wicking rate, Φ_w
Rahman *et al.* [2]	$q''_{CHF} = q''_{Zuber} + \alpha_{fit} \rho_l h_{fg} \dot{V}''$ *	Empirical	Wicking flux, ϕ''_w
Kim *et al.* [20]	$q''_{CHF} = \alpha_{fit,1} q''_{Kandlikar} + \alpha_{fit,2} \rho_l \left(1-\phi\right) W^2 / \lambda_{RT}^2$ *	Empirical	Wicking factor, W
Kwak *et al.* [13]	$q''_{CHF} = q''_{flat} + \alpha_{fit,1} \left(\gamma L_C\right)^{\alpha_{fit,2}}$ *	Empirical	Wicking capability, γL_C
Li *et al.* [21]	$q''_{CHF} = q''_{Kandlikar} + \alpha_{fit} h_{fg} H \sqrt{\frac{P-D}{P^2} g \cos\theta \rho_l \Delta\rho_{lv}} \frac{\left(P-D\right)}{\sin\psi P^2}$ *	Semi-analytical	-
Dhillon *et al.* [10]	$q''_{CHF} = \rho_s C_s \min\left(t_s, \sqrt{\alpha \tau_w}\right)\left(T_{crit} - T_o\right)\left[\left(\frac{4\Delta\rho_{lv} g^3}{\sigma}\right)^{1/4}\left(1-\tau_r\right) + \max\left(0, \tau_w^{-1}\right)\right]$	Analytical	Wicking time scale, $\tau_w = \mu\sigma / \left(2\Delta\rho_{lv} g P_C K_B\right)$
Kim *et al.* [8]	$q''_{CHF} = \rho_l h_{fg} \left(\Phi_g + \Phi_w\right) / A_w$	Analytical	Volumetric wicking rate, $\Phi_w = P_C W H^3 / \left(a\mu L_C\right)$
Xiao *et al.* [23]	N/A		Propagation coefficient, $G = \sqrt{2 P_C K_B}$
Allred *et al.* [24]	N/A		Superhydrophilicity metric, $\omega = P_C K H$

* α_{fit} is a generic symbol representing fitting parameters used in existing models [2,13,17,20,21].

2. Theoretical Model

2.1 Coupled wicking and evaporation mechanism for CHF enhancement

In contrast with existing wicking-based models that relate CHF only to the wicking characteristics of surface structures, the present work explores the coupled roles of wicking and evaporation in determining the critical heat flux. Figure 1 (a) shows a schematic drawing of a vapor bubble on a structured surface during boiling, with the inset illustrating wicking and evaporation in the liquid layer underneath the bubble. Driven by capillary wicking, liquid is pumped radially inward from the bulk surrounding pool, through the microstructures and to the edge of a circular dry spot centered under the bubble. Simultaneously, evaporation occurs from the menisci at the liquid-vapor interface as shown in the inset. Mass balance requires that the evaporation rate from the liquid layer is equal to the wicking rate. This balance determines the diameter of the dry spot underneath the bubble, which in turn governs the wicking rate because the pressure gradient that drives the flow in the liquid layer depends on the wicking length (*i.e.*, the distance from the bulk liquid to the edge of the dry spot). If the dry spot diameter becomes larger, this leads to a smaller wicking length and therefore larger wicking rate, but also results in a smaller evaporative area and thus smaller evaporation rate. Consequently, a balance between wicking and evaporation will be reached at some dry spot diameter for a given surface heat flux.

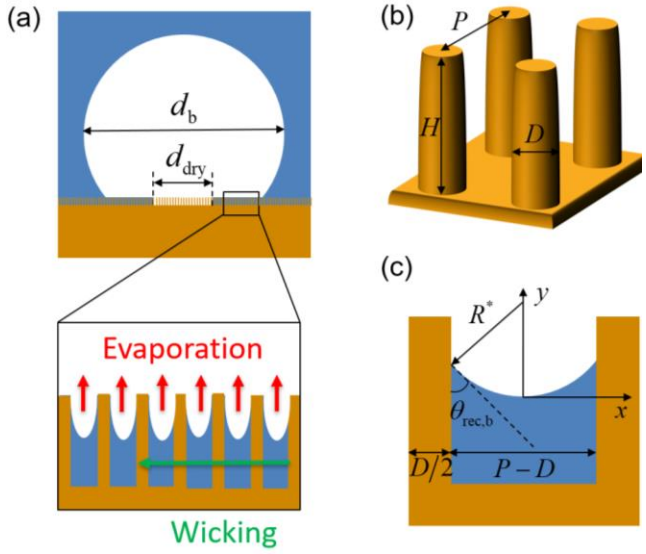

Figure 1. Schematic drawings of (a) a vapor bubble on a structured surface during pool boiling with inset view of the liquid layer underneath the bubble, (b) a unit cell of a square micropillar array on the structured surface, and (c) a side view of the evaporating meniscus formed between two pillars within the unit cell.

Using this framework, we are able to study two key mechanisms that have not been previously considered in existing analytical models for CHF on structured surfaces. The first of these is the competition between wicking and evaporation from the liquid layer underneath the bubble; based on this balance, the dry spot diameter, and in turn the CHF, is calculated. The second issue addressed is that existing CHF models assume linear wicking behavior, whereas in reality, liquid is wicked radially underneath the bubble during boiling. Allred *et al.* [24] noted that the volumetric rate of radial wicking does not follow the Washburn-type square-root law as in linear wicking. Therefore, in order to accurately predict CHF during pool boiling, the radial wicking of liquid in structured surfaces must be considered.

2.2 Model formulation

Two components contribute to the critical heat flux on structured surfaces: the CHF for a flat surface $q''_{\mathrm{CHF,f}}$, and the structure-induced CHF enhancement $q''_{\mathrm{CHF,s}}$, such that

$$q''_{\mathrm{CHF}} = q''_{\mathrm{CHF,f}} + q''_{\mathrm{CHF,s}} \tag{1}$$

In the present work, the Dhir-Liaw model [25] that accounts for the effect of the contact angle on CHF is used to calculate $q''_{\mathrm{CHF,f}}$. The apparent contact angle on structured surfaces is calculated using the equilibrium contact angle at room temperature [26], and is substituted into Dhir and Liaw's model. The structure-induced CHF enhancement $q''_{\mathrm{CHF,s}}$ is calculated based on the competition between wicking and evaporation.

Following the mechanism introduced in Section 2.1, the balance between wicking and evaporation requires the volumetric rate of wicking to equal the volumetric rate of evaporation following $\Phi_{\mathrm{w}} = \Phi_{\mathrm{e}}$. The volumetric wicking rate Φ_{w} is calculated based on inward radial flow in a porous medium. The continuity equation gives $\frac{1}{r}\frac{\partial}{\partial r}\left(ru_r\right) = 0$. The momentum balance is described with Brinkman's equation [27]

$$\frac{\mu}{\varepsilon}\left[\frac{\partial^2 u_r}{\partial z^2} + \frac{1}{r}\frac{\partial}{\partial r}\left(r\frac{\partial u_r}{\partial r}\right)\right] - \frac{dP_{\mathrm{l}}}{dr} - \frac{\mu}{K}u_r = 0 \tag{2}$$

At the edge of the bubble ($r = d_{\mathrm{b}}/2$), the liquid pressure is equal to the bulk liquid pressure, $P\big|_{r=d_{\mathrm{b}}/2} = P_0$. At the dry spot, liquid pressure deviates from the bulk liquid pressure according to

$P\big|_{r=d_{\mathrm{dry}}/2} = P_0 - P_{\mathrm{C}}$. A non-slip boundary condition is applied on the base surface ($u_r\big|_{z=0} = 0$) and a free surface boundary is applied at the liquid-vapor interface ($\partial u_r/\partial z\big|_{z=H} = 0$). The mean wicking front velocity dR/dt is determined as $\frac{dR}{dt} = \frac{1}{\varepsilon H}\int_0^H u_r\left(z,R\right)dz$, and the volume of the liquid wicked into the structures at any instant is $V_{\mathrm{w}} = \varepsilon\pi H\left(d_{\mathrm{b}}^2/4 - R^2\right)$. The volumetric wicking rate, $\Phi_{\mathrm{w}} = dV_{\mathrm{w}}/dt$, is therefore derived as

$$\Phi_{\mathrm{w}} = \frac{2\pi P_{\mathrm{C}} KH}{\mu \ln\left(d_{\mathrm{b}}/d_{\mathrm{dry}}\right)}\left[1 - \frac{\tanh\left(\sqrt{\varepsilon/K}H\right)}{\sqrt{\varepsilon/K}H}\right] \tag{3}$$

The details of the derivation of Equation (3) are included in Section S1 of the Supplementary Material. While *K* represents the viscous resistance from the micropillars, the term in the square brackets, $\left[1-\tanh\left(\sqrt{\varepsilon/K}H\right)\Big/\left(\sqrt{\varepsilon/K}H\right)\right]$, accounts for the viscous resistance from the base surface. An effective permeability defined as $K_{\mathrm{B}} = K\left[1-\tanh\left(\sqrt{\varepsilon/K}H\right)\Big/\left(\sqrt{\varepsilon/K}H\right)\right]$ is introduced to represent the resistance to the flow from both the micropillars and the base surface. We note that the volumetric wicking rate depends on the departure bubble diameter d_{b}. Based on the balance between surface tension forces and buoyancy, the departure bubble diameter increases with increasing receding contact angle [28, 29]. While this trend is clearly observed at low heat fluxes in experiments, it becomes less obvious at higher heat fluxes [30]. Therefore, the effect of the receding contact angle on departure bubble diameter during CHF is not considered in the present work. The departure bubble diameter is approximated as $d_{\mathrm{b}} = \lambda_{\mathrm{RT}}/2$ [22], where λ_{RT}, the critical wavelength of the Rayleigh-Taylor instability, is defined as $\lambda_{\mathrm{RT}} = 2\pi\sqrt{\sigma_{\mathrm{lv}}/g\Delta\rho_{\mathrm{lv}}}$ [1].

It is evident from Equation (3) that the volumetric wicking rate is dependent on the details of the structured surface as well as the dry spot diameter d_{dry}. A characteristic wicking rate that is independent of the dry spot diameter is introduced as $\Phi_{\mathrm{w,ch}} = \Phi_{\mathrm{w}}\ln\left(d_{\mathrm{b}}/d_{\mathrm{dry}}\right)$. Allred *et al.* [24] defined the superhydrophilicity metric, $\omega = P_{\mathrm{C}}KH$, where the capillary pressure P_{C} drives the liquid flow and the inverse of the permeability K^{-1} represents the strength of the viscous resistance to the flow from the structures. Here we extend the definition of the superhydrophilicity metric to

include the effect of viscous resistance from the base surface, as $\omega^* = P_C K_B H$. Using this modified superhydrophilicity metric, the characteristic wicking rate can be represented as $\Phi_{w,ch} = 2\pi\omega^* / \mu$. Figure 2 plots the critical heat flux q''_{CHF} as a function of the characteristic wicking rate $\Phi_{w,ch}$ for experimental data from the literature on pool boiling on square micropillar arrays [2, 3, 7, 11]. The wetting properties and geometric dimensions of the surfaces used in these references are summarized in Section S2 of the Supplementary Material. These properties are used to calculate the capillary pressure P_C and effective permeability using the models described in Section 2.3 below. A general monotonically increasing trend in q''_{CHF} can be observed with increasing $\Phi_{w,ch}$, demonstrating wicking to be a key mechanism that enhances the critical heat flux. Each study included in the figure considered a different structure, leading to the observed scatter in the data. This scatter indicates that solely considering wicking enhancement is not sufficient to capture the exact relationship between CHF and the surface structures.

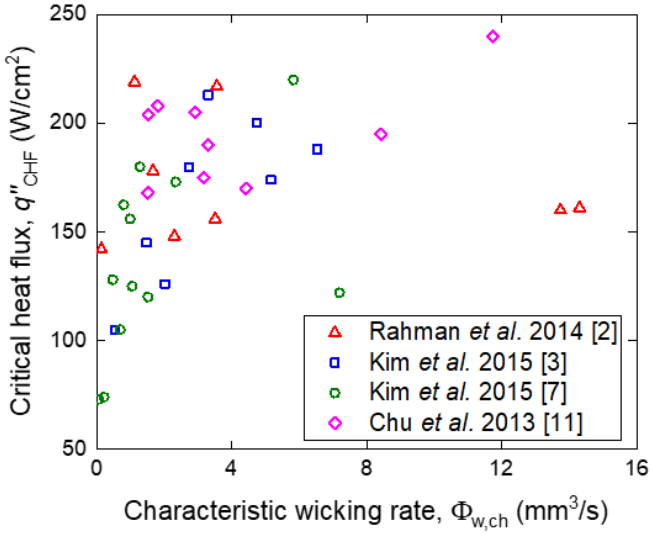

Figure 2. Critical heat flux as a function of the characteristic wicking rate for water boiling on square micropillar arrays.

The evaporation rate of the liquid layer underneath the bubble can be calculated as $\Phi_e = \pi\left(d_b^2 - d_{dry}^2\right)\phi''_{e,avg} / 4$, where $\phi''_{e,avg}$ is the average volumetric evaporation flux from the top

surface of the liquid layer. Based on the balance between wicking and evaporation, $\Phi_w = \Phi_e$, Equation (3) gives

$$\frac{2\pi K P_C H}{\mu \ln\left(d_b/d_{dry}\right)}\left[1-\frac{\tanh\left(\sqrt{\varepsilon/K}H\right)}{\sqrt{\varepsilon/K}H}\right]=\frac{\pi}{4}\left(d_b^2-d_{dry}^2\right)\phi''_{e,avg} \quad . \tag{4}$$

The wicking flux ϕ''_w and the evaporation flux ϕ''_e are defined by scaling the volumetric wicking rate and evaporation rate with the area over which the effect is felt (*viz.* the bubble footprint) as $\phi''_w = \Phi_w / d_b^2$ and $\phi''_e = \Phi_e / d_b^2$, respectively. Following the definition of the characteristic wicking rate, a characteristic wicking flux is defined as $\phi''_{w,ch} = 2\pi\omega^* / \left(\mu d_b^2\right)$. A characteristic evaporation flux is defined as the maximum evaporation flux in the limit of $d_{dry} \to 0$, giving $\phi''_{e,ch} = \pi\phi''_{e,avg}/4$. Using the definition of the modified superhydrophilicity metric and the effective permeability, Equation (3) is reduced to $\Phi_w = 2\pi\omega^* / \ln\left(d_b/d_{dry}\right)$. The wicking flux can be obtained as $\phi''_w = \phi''_{w,ch} / \ln\left(d_b/d_{dry}\right)$ and the wicking heat flux is therefore $q''_w = \rho_l h_{fg} \phi''_{w,ch} / \ln\left(d_b/d_{dry}\right)$. Similarly, the evaporation heat flux can be obtained as $q''_e = \rho_l h_{fg} \phi''_{e,ch}\left(1-d_{dry}^2/d_b^2\right)$. Using $\phi''_{w,ch}$ and $\phi''_{e,ch}$ to denote the terms on the L.H.S. and R.H.S. of Equation (4), respectively, Equation (4) is reduced to

$$\frac{\phi''_{w,ch}}{\phi''_{e,ch}} = \left[1-\left(\frac{d_{dry}}{d_b}\right)^2\right]\ln\left(\frac{d_b}{d_{dry}}\right) \tag{5}$$

Equation (5) clearly shows the effect of the competition between wicking and evaporation on the dry spot diameter. The R.H.S. of Equation (5) is a monotonically decreasing function of the scaled dry spot diameter, d_{dry}/d_b. Therefore, d_{dry}/d_b increases with the ratio of the characteristic wicking flux to the characteristic evaporation flux, $\phi''_{w,ch}/\phi''_{e,ch}$. When $\phi''_{w,ch}/\phi''_{e,ch} >> 1$, wicking dominates and the dry spot diameter approaches zero ($d_{dry}/d_b \to 0$). When $\phi''_{w,ch}/\phi''_{e,ch} << 1$, wicking is not sufficient to maintain the liquid layer underneath the bubble, and the dry spot approaches the edge of the bubble ($d_{dry}/d_b \to 1$).

The critical dry spot diameter that satisfies the balance between wicking and evaporation, d_{dry}^{*} can be determined by solving Equation (5). With the calculated d_{dry}^{*}, the CHF enhancement is determined by setting $q''_{\mathrm{CHF,s}} = q''_{\mathrm{w}}\left(d_{\mathrm{dry}}^{*}\right) = q''_{\mathrm{e}}\left(d_{\mathrm{dry}}^{*}\right)$, or

$$q''_{\mathrm{CHF,s}} = \frac{\rho_{\mathrm{l}} h_{\mathrm{fg}} \phi''_{\mathrm{w,ch}}}{\ln\left(d_{\mathrm{b}} / d_{\mathrm{dry}}^{*}\right)} = \rho_{\mathrm{l}} h_{\mathrm{fg}} \phi''_{\mathrm{e,ch}} \left[1 - \left(\frac{d_{\mathrm{dry}}^{*}}{d_{\mathrm{b}}}\right)^{2}\right] \tag{6}$$

With $q''_{\mathrm{CHF,s}}$ known, CHF can be readily calculated using Equation (1).

2.3 Superhydrophilicity metric calculation

The characteristic wicking flux $\phi''_{\mathrm{w,ch}}$ depends on the modified superhydrophilicity metric, ω^{*}, which is a function of the capillary pressure P_{C} and the effective permeability K_{B}. The capillary pressure P_{C} is calculated as the free energy change per unit volume for liquid wetting the surface structures, *i.e.*, $P_{\mathrm{C}} = \Delta E / \Delta V$ [23]. For a square micropillar array such as the case illustrated in Figure 1 (b), the capillary pressure is calculated as follows

$$P_{\mathrm{C}} = \frac{\sigma_{\mathrm{lv}} D}{P^{2} - \pi D^{2}/4} \pi r_{\mathrm{s}} \cos\theta_{\mathrm{equ,b}} - \frac{\sigma_{\mathrm{lv}}}{H}\left(\cos\theta_{\mathrm{equ,b}} - 1\right) r_{\mathrm{area}} \tag{7}$$

The factor r_{area} is used to correct the wetted surface area when the micropillar array is not dense enough to support a complete meniscus. For dense structures, $H > \left(P - D\right) / \left(2\cos\theta_{\mathrm{rec,b}}\right)$, and a complete continuous meniscus can be formed on the structure leading to $r_{\mathrm{area}} = 1$. For sparse structures, r_{area} is approximated as $r_{\mathrm{area}} = \min\left\{1, 1 - \frac{\pi P^{2}}{4\left(P^{2} - \pi D^{2}/4\right)}\right\}$. A variety of models have been proposed to predict the permeability of square micropillar arrays [23, 31, 32], among which the one by Yazdchi *et al.* [32] has been shown to agree with experimental results for square micropillar arrays having both high and low porosities [33]. The capillary pressure calculated based on Equation (7) and Yazdchi *et al.*'s permeability model are validated against experiments from the literature [20, 24]. The detailed derivation of Equation (7) and a comparison of the wicking characteristics with experiments are provided in Section S3 of the Supplementary Material.

2.4 Average evaporation flux calculation

The characteristic evaporation flux $\phi''_{e,ch}$ depends on the average evaporation flux from the meniscus in the surface structures $\phi''_{e,avg}$. Figure 1 (c) shows a two-dimensional view of the liquid layer in a unit cell of a square micropillar array underneath a vapor bubble. The conduction resistance in the solid pillar is neglected due to its high thermal conductivity. Therefore, an isothermal condition is assumed along the pillar surface. The conduction path from the base surface to the liquid-vapor interface is also neglected as the thermal conductivity of the solid pillar is much higher than that of the liquid. The dominant thermal resistance includes the conduction resistance in the liquid and the liquid-vapor interfacial resistance. The volumetric evaporation flux based on an equilibrium meniscus is calculated as

$$\phi''_{e,avg,equ} = \frac{1}{\rho_l h_{fg} P^2} \int_0^{R^*(1-\sin\theta_{rec,b})} \frac{\pi\left(D+2\delta(y)\right)h_{lv}\left(T_s-T_v\right)}{1+\left(h_{lv}/k_l\right)\ln\left(\left(D+2\delta(y)\right)/D\right)\left(D/2+\delta(y)\right)}dy \tag{8}$$

where δ is the liquid thickness perpendicular to the pillar surface. In Equation (8), the evaporation heat transfer coefficient h_{lv} is defined as $h_{lv} = \left(\frac{2\hat{\sigma}}{2-\hat{\sigma}}\right)\frac{h_{fg}^2\rho_v}{T_v}\left(\frac{M}{2\pi R_u T_v}\right)^{1/2}$.

We note that Equation (8) calculates the volumetric evaporation rate based on the surface profile of an equilibrium meniscus. However, it is known that the surface profile of an evaporating meniscus deviates from that of the equilibrium meniscus. In Section S4 of the Supplementary Material, the thin film evaporation model developed by Wang *et al.* [34] is used to analyze the nonequilibrium effect on evaporation flux of a meniscus. A correction factor is proposed to account for the effect of the nonequilibrium meniscus, which for water on hydrophilic surfaces with zero receding contact angle is $\left(\phi''_{e,avg,equ}-\phi''_{e,avg}\right)/\phi''_{e,avg} = 0.12\ln\left(R^*/\delta_c\right)$, where $\phi''_{e,avg,equ}$ and $\phi''_{e,avg}$ are the volumetric evaporation flux calculated based on an equilibrium meniscus and an evaporating meniscus, respectively, and δ_c is the critical film thickness where the liquid-vapor interfacial resistance is comparable with the conduction resistance, following $\delta_c = k_l/h_{lv}$. Details of the nonequilibrium correction can be found in Section S4 of the Supplementary Material.

3. Results and Discussion

3.1 Competition between wicking and evaporation

The structure-induced CHF enhancement $q''_{\mathrm{CHF,s}}$ is a function of the size of the dry spot underneath the bubble, which is determined based on the balance between wicking and evaporation from the liquid layer under the bubble, as discussed in Section 2.2. To show the role of wicking and evaporation in determining the size of the dry spot, the wicking heat flux q''_{w} (blue dashed curve) and the evaporation heat flux q''_{e} (red solid curve) are shown in Figure 3 as a function of the scaled dry spot diameter $d_{\mathrm{dry}}/d_{\mathrm{b}}$, for water boiling on a square micropillar array with micropillar diameter D = 5 μm, pitch P = 10 μm, and height H = 20 μm. The equilibrium and receding contact angles at the boiling point are taken as $\theta_{\mathrm{equ,b}}$ = 40° and $\theta_{\mathrm{rec,b}}$ = 0°, respectively. The wall superheat is $\left(T_{\mathrm{s}}-T_{\mathrm{v}}\right)=25$ K. Thermophysical properties of water at the boiling point (*viz.* 100 °C at atmospheric pressure) are used in the present study, including surface tension σ = 0.0589 J/m^2, viscosity μ = 2.822 x 10^{-4} Pa·s, enthalpy of vaporization h_{fg} = 2.2×10^6 J/kg, liquid thermal conductivity k_{l} = 0.677 Wm/K, liquid density ρ_{l} = 958 kg/m^3, and vapor density ρ_{v} = 0.554 kg/m^3. The accommodation coefficient of water is usually in the range of 0.02 – 0.04 [35], and a value of $\hat{\sigma}$ = 0.03 is used here. The wicking and evaporation heat fluxes are functions of the dry spot diameter following $q''_{\mathrm{w}}=\rho_{\mathrm{l}}h_{\mathrm{fg}}\phi''_{\mathrm{w,ch}}\left/\ln\left(d_{\mathrm{b}}/d_{\mathrm{dry}}\right)\right.$ and $q''_{\mathrm{e}}=\rho_{\mathrm{l}}h_{\mathrm{fg}}\phi''_{\mathrm{e,ch}}\left(1-d^2_{\mathrm{dry}}/d^2_{\mathrm{b}}\right)$, respectively, where the characteristic flux $\phi''_{\mathrm{w,ch}}$ and the characteristic evaporation flux $\phi''_{\mathrm{e,ch}}$ depend on the structure geometry and wettability. As shown in Figure 3, the wicking heat flux q''_{w} increases with the scaled dry spot diameter $d_{\mathrm{dry}}/d_{\mathrm{b}}$, while the evaporation heat flux q''_{e} decreases with $d_{\mathrm{dry}}/d_{\mathrm{b}}$. As the dry spot diameter increases, the distance that the liquid must travel from the bulk surrounding pool to the dry spot decreases, leading to a smaller viscous resistance and therefore a larger wicking heat flux. On the other hand, the increasing dry spot diameter leads to a smaller area for evaporation and therefore a smaller evaporation heat flux. A critical dry spot diameter d^*_{dry} is determined from the wicking and evaporation balance $q''_{\mathrm{w}}\left(d^*_{\mathrm{dry}}\right)=q''_{\mathrm{e}}\left(d^*_{\mathrm{dry}}\right)$.

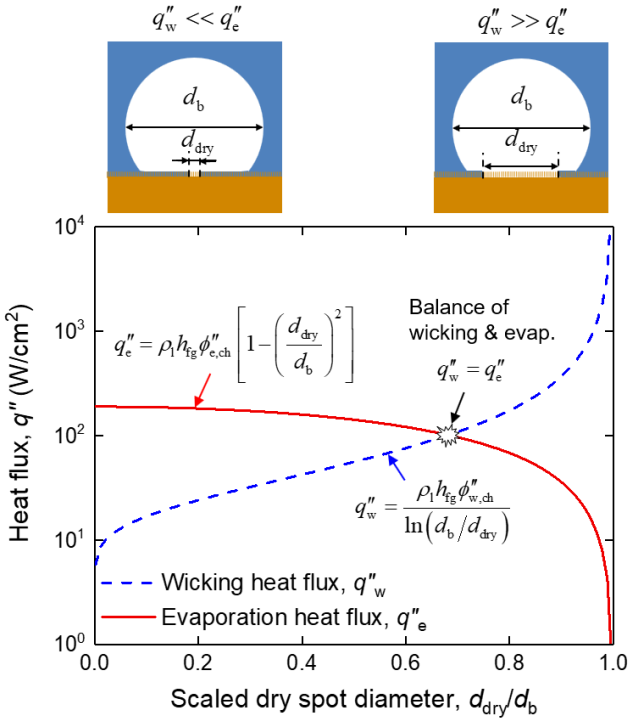

Figure 3. Comparison between evaporation heat flux q''_e and wicking heat flux q''_w as a function of the scaled dry out diameter d_{dry}/d_b for water boiling on a square micropillar array (D = 5 μm, P = 10 μm, H = 20 μm, $\theta_{equ,b}$ = 40°, $\theta_{rec,b}$ = 0°, and $(T_s - T_v) = 25$ K).

While Figure 3 shows how the critical dry spot diameter d^*_{dry} is determined for a specific structure geometry and wettability (and thereby for fixed $\phi''_{w,ch}$ and $\phi''_{e,ch}$), it is also important to understand the effect of the wicking and evaporation characteristics on the resulting CHF. To this end, Figure 4 shows a contour plot of the structure-induced CHF enhancement $q''_{CHF,s}$ with varying characteristic wicking flux $\phi''_{w,ch}$ and characteristic evaporation flux $\phi''_{e,ch}$. When $\phi''_{w,ch}$ is much larger than $\phi''_{e,ch}$, the contour lines become parallel to the $\phi''_{w,ch}$ axis, indicating that the CHF enhancement $q''_{CHF,s}$ is independent of the characteristic wicking flux $\phi''_{w,ch}$. This trend can be readily explained with Equation (5) and Equation (6) in Section 2.2. In the limit of $\phi''_{w,ch}/\phi''_{e,ch} \to \infty$, wicking is strong enough to deliver liquid to the center of the bubble, leading to $d_{dry}/d_b \to 0$, based on Equation (5). Consequently, in this limit, the CHF enhancement $q''_{CHF,s}$ converges to

$\rho_l h_{fg} \phi''_{e,ch}$ based on Equation (6). Further increase in the characteristic wicking flux will not lead to improvement in $q''_{CHF,s}$. In the limit of $\phi''_{w,ch} / \phi''_{e,ch} \to 0$, on the other hand, the wicking flux is not sufficient to support evaporation from the liquid layer. As a result, the dry spot will expand to the edge of the bubble ($d_{dry} / d_b \to 1$), leaving no liquid layer underneath the bubble. Under this condition, the contour lines of $q''_{CHF,s}$ approach the $\phi''_{e,ch}$ axis asymptotically, *viz.* $q''_{CHF,s} \to 0$. Based on Figure 4, it is evident that both large $\phi''_{w,ch}$ and large $\phi''_{e,ch}$ are required to achieve highly enhanced CHF using structured surfaces.

Three representative experimental results for CHF enhancement $q''_{s,exp}$ [2, 3] are plotted in Figure 4, where the $\phi''_{w,ch}$ and $\phi''_{e,ch}$ are calculated based on the wetting properties and geometric dimensions reported in these studies. The data points with $q''_{s,exp}$ = 106 W/cm^2 and $q''_{s,exp}$ = 104 W/cm^2 correspond to square micropillar arrays with D = 4 μm, P = 7 μm, H = 16 μm, and D = 15 μm, P = 21 μm, H = 32 μm, respectively [2]. The structure that yields $q''_{s,exp}$ = 106 W/cm^2 falls in the regime where $q''_{s,exp}$ is significantly limited by wicking. The data point with $q''_{s,exp}$ = 61 W/cm^2 corresponds to a square micropillar array with D = 80 μm, P = 160 μm, and H = 20 μm [3]. This structure falls in the regime where $q''_{s,exp}$ is strongly limited by evaporation and converges to $\rho_l h_{fg} \phi''_{e,ch}$. The three representative experimental data points demonstrate a range of surface structures used in pool boiling experiments that fall into either the wicking-limited CHF regime or the evaporation-limit regime.

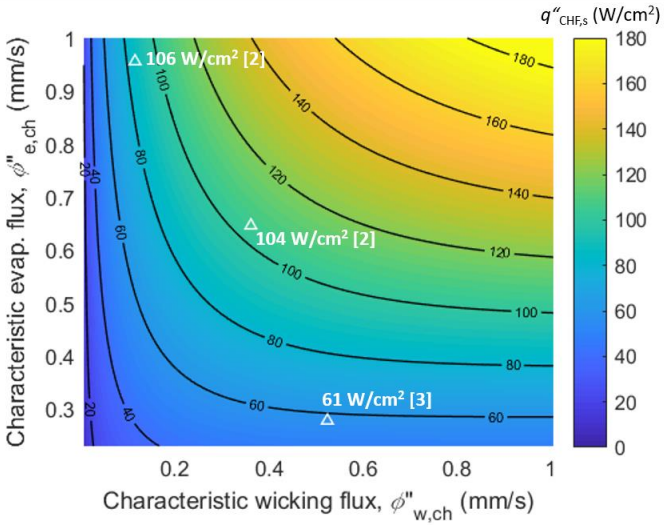

Figure 4. Dependence of the structure-induced CHF enhancement $q''_{\mathrm{CHF,s}}$ on the characteristic evaporation flux $\phi''_{\mathrm{e,ch}}$ and the characteristic wicking flux $\phi''_{\mathrm{w,ch}}$. The white triangles denote three representative cases of experimental CHF enhancement data from the literature: $q''_{\mathrm{s,exp}}$ = 106 W/cm^2 [2], $q''_{\mathrm{s,exp}}$ = 104 W/cm^2 [2], and $q''_{\mathrm{s,exp}}$ = 61 W/cm^2 [3].

3.2 Microstructure design criteria for enhanced CHF

Using the CHF model developed here, a parametric study is performed to investigate the effect of structure geometry on the CHF enhancement, using the square micropillar array shown in Figure 1 (b). The geometry of the micropillar array can be captured using the size of the micropillars and two ratios including the diameter-to-pitch ratio D/P, and the height-to-pitch ratio H/P. Water is used as the working fluid, with thermophysical properties as listed in Section 3.1. The wall superheat is fixed at $\left(T_{\mathrm{s}}-T_{\mathrm{v}}\right)=25$ K. The effect of the nonequilibrium correction on the CHF enhancement is described in Section S5 of the Supplementary Material.

To understand the effect of the micropillar dimensions on CHF, Figure 5 (a) plots the structure-induced CHF enhancement $q''_{\mathrm{CHF,s}}$ as a function of the micropillar pitch P, for a fixed ratio of the micropillar diameter, pitch, and height, D:P:H = 1:2:4. As shown in Figure 5 (a), an optimal micropillar pitch exists at P_{opt} = 23.4 μm where $q''_{\mathrm{CHF,s}}$ is maximized. The structure-induced CHF enhancement $q''_{\mathrm{CHF,s}}$ increases with the micropillar pitch P up to an optimal pitch P_{opt} at which

$q''_{\mathrm{CHF,s}}$ is maximum, and then decreases with P for $P > P_{\mathrm{opt}}$. In order to understand the underlying mechanism of this optimal pitch for a fixed D:P:H ratio, Figure 5 (b) shows the characteristic wicking flux $\phi''_{\mathrm{w,ch}}$ (blue dashed line) and the characteristic evaporation flux $\phi''_{\mathrm{e,ch}}$ (red solid line) versus the micropillar pitch P. An increase in structure size (represented by micropillar pitch P) leads to larger $\phi''_{\mathrm{w,ch}}$ and smaller $\phi''_{\mathrm{e,ch}}$. The characteristic wicking flux $\phi''_{\mathrm{w,ch}}$ scales with the modified superhydrophilicity metric ω^* as $\phi''_{\mathrm{w,ch}} = 2\pi\omega^* / \left(\mu d_{\mathrm{b}}^2\right)$, where $\omega^* = P_{\mathrm{C}} K_{\mathrm{B}} H$. Because the capillary pressure P_{C} scales with the inverse of the structure size, and the effective permeability K_{B} scales with the square of the structure size, $\phi''_{\mathrm{w,ch}}$ increases quadratically with the structure size. Conversely, the characteristic evaporation flux $\phi''_{\mathrm{e,ch}}$ decreases with structure size due to the larger conduction resistance. Therefore, it is clear that the optimal pitch at which the maximum $q''_{\mathrm{CHF,s}}$ is reached results from the competition between wicking and evaporation in the liquid layer. This optimal size separates the structure dimension into two regimes, *viz.* the wicking-limited regime ($P < P_{\mathrm{opt}}$) where $q''_{\mathrm{CHF,s}}$ increases with $\phi''_{\mathrm{w,ch}}$, and the evaporation-limited regime ($P > P_{\mathrm{opt}}$) where a further increase in $\phi''_{\mathrm{w,ch}}$ does not lead to enhancement in $q''_{\mathrm{CHF,s}}$. Because the ratio of D:P:H is fixed, the micropillar diameter D and height H scale with the pitch P, and P_{opt} represents the optimal size of the square micropillar array under this constraint.

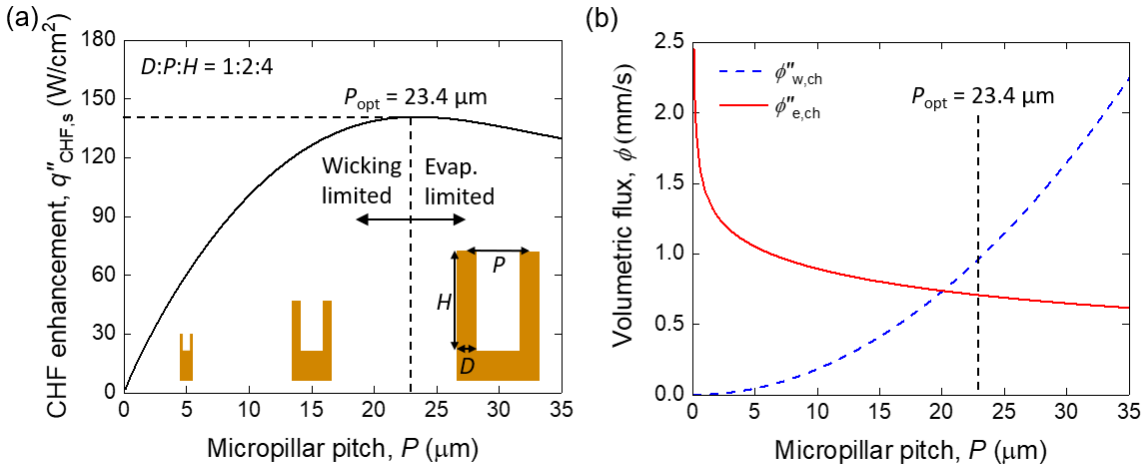

Figure 5. Effect of the micropillar size on CHF showing (a) the CHF enhancement $q''_{\mathrm{CHF,s}}$ and (b) the characteristic wicking flux $\phi''_{\mathrm{w,ch}}$ and characteristic evaporation flux $\phi''_{\mathrm{e,ch}}$ as a function of the micropillar pitch P for water boiling on square micropillar arrays (D:P:H = 1:2:4).

While the above discussion on optimal structure size is based on fixed diameter-to-pitch and height-to-pitch ratios, the dependence of CHF enhancement on these ratios is now explored. Figure 6 (a) plots the structure-induced CHF enhancement $q''_{\mathrm{CHF,s}}$ as a function of the diameter-to-pitch ratio D/P of a square micropillar array. The height-to-pitch ratio is fixed at H/P = 2:1, and the pitch is fixed at P = 10 μm. It is evident from the figure that $q''_{\mathrm{CHF,s}}$ approaches zero in the limit of $D/P \to 0$ as well as of $D/P \to 1$ because the micropillar array is reduced to a flat surface in both limits. Figure 6 (b) plots the characteristic wicking flux $\phi''_{\mathrm{w,ch}}$ (blue dashed line) and characteristic evaporation flux $\phi''_{\mathrm{e,ch}}$ (red solid line) versus the diameter-to-pitch ratio D/P. As D/P increases, the capillary pressure P_{C} increases due to the smaller radius of curvature ($R^* = \left(P-D\right)\Big/\left(2\cos\theta_{\mathrm{rec,b}}\right)$), while the flow permeability K_{B} decreases due to smaller porosity ($\varepsilon = 1-\pi D^2\Big/\left(4P^2\right)$). The competition between the capillary pressure and the viscous resistance leads to a maximum $\phi''_{\mathrm{w,ch}}$ at an intermediate diameter-to-spacing ratio of $(D/P)_{\mathrm{w}}$ = 0.28. As D/P increases, the evaporative heat transfer area decreases, leading to a larger liquid-vapor interfacial resistance. On the other hand, as D/P increases, the liquid film thickness in the meniscus decreases, leading to reduced conduction resistance. This competition between the conduction resistance and the interfacial resistance leads to a maximum $\phi''_{\mathrm{e,ch}}$ at $(D/P)_{\mathrm{e}}$ = 0.50. Because the structure-induced CHF enhancement is affected by both wicking and evaporation in the liquid layer, the optimal diameter-to-pitch ratio for the maximum $q''_{\mathrm{CHF,s}}$ is found to be between $(D/P)_{\mathrm{w}}$ = 0.28 and $(D/P)_{\mathrm{e}}$ = 0.50, at $(D/P)_{\mathrm{opt}}$ = 0.39. Existing studies have reported the competition between the capillary pressure and the viscous resistance in determining the wicking flux [23] and CHF [10]. Our model further reveals that the competition between the conduction resistance and interfacial resistance of evaporation in the liquid layer is also an important mechanism that leads to a non-monotonic relation between CHF and the diameter-to-pitch ratio, which is expected to have a stronger influence on CHF in the evaporation-limited regime.

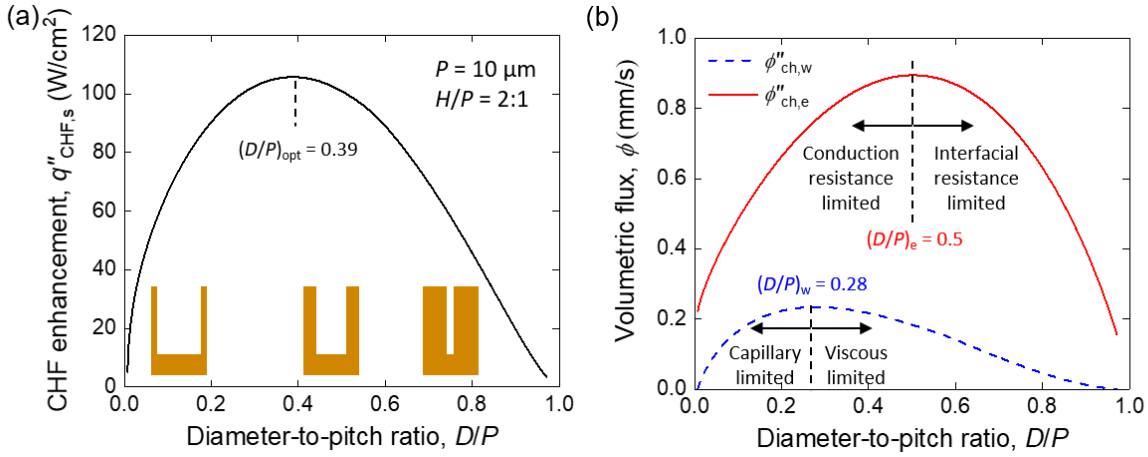

Figure 6. Effect of the diameter-to-pitch ratio D/P on CHF showing (a) the CHF enhancement $q''_{\mathrm{CHF,s}}$ and (b) the characteristic wicking flux $\phi''_{\mathrm{w,ch}}$ and characteristic evaporation flux $\phi''_{\mathrm{e,ch}}$ as functions of the scaled pillar diameter D/P for water boiling on square micropillar arrays (P = 10 μm and H/P = 2:1).

The effect of the height-to-pitch ratio H/P of the micropillar array on CHF enhancement is also investigated, as shown in Figure 7 (a) for a fixed D/P of 1:2 and pitch of P = 10 μm. The value of $q''_{\mathrm{CHF,s}}$ increases monotonically with the height-to-pitch ratio H/P and asymptotes toward a constant $q''_{\mathrm{CHF,s}}$ (dashed line) at high height-to-pitch ratios. The dashed line in Figure 7 (a) represents the evaporation limit of CHF, calculated using Equation (6) at $d_{\mathrm{dry}}/d_{\mathrm{b}} \to 0$, *viz.* $q''_{\mathrm{CHF,s}} = \rho_{\mathrm{l}} h_{\mathrm{fg}} \phi''_{\mathrm{e,ch}}$, which gives $q''_{\mathrm{CHF,s}}$ = 188.5 W/cm^2 for P = 20 μm and D/P = 0.5. In order to understand the trend in Figure 7 (a), the characteristic wicking flux $\phi''_{\mathrm{w,ch}}$ (blue dashed curve) and characteristic evaporation flux $\phi''_{\mathrm{e,ch}}$ (red solid curve) are plotted in Figure 7 (b) versus the height-to-pitch ratio H/P. While $\phi''_{\mathrm{w,ch}}$ increases nearly linearly with H/P, the characteristic evaporation flux $\phi''_{\mathrm{e,ch}}$ is not affected by H/P over the range of parameters investigated. The characteristic wicking flux scales linearly with the superhydrophilicity metric as $\phi''_{\mathrm{w,ch}} = 2\pi\omega^* / \left(\mu d_{\mathrm{b}}^2\right)$ where $\omega^* = P_{\mathrm{C}} K_{\mathrm{B}} H$. Because the capillary pressure P_{C} and effective permeability K_{B} only weakly depend on the micropillar height H, the characteristic wicking flux scales nearly linearly with H. Such a near-linear trend between wicking flux and structure height

was also observed in the experiments of Adera *et al.* [36] on wicking-driven evaporation in square micropillars. As for $\phi''_{e,ch}$, evaporation is not affected by the micropillar height unless the height is so small as to not support a complete meniscus. As the smallest micropillar height investigated here still satisfies the dense structure assumption ($H > (P-D)/(2\cos\theta_{rec,b})$), the characteristic evaporation flux is independent of the micropillar height. As a result of the trends in the characteristic wicking and evaporation fluxes, $q''_{CHF,s}$ increases with the scaled micropillar height due to enhanced wicking. However, as discussed in Section 3.1, $q''_{CHF,s}$ is limited by evaporation in the regime where $\phi''_{w,ch} >> \phi''_{e,ch}$. As shown in Figure 7 (b), when the micropillar height is large, $\phi''_{w,ch} >> \phi''_{e,ch}$, and $q''_{CHF,s}$ becomes limited by evaporation, leading to the asymptotic increase in the CHF enhancement in this regime shown in Figure 7 (a). We note that this discussion on the effect of structure height on CHF enhancement assumes a condition where the structure is much smaller than the bubble (*viz.* $H << d_b$). When the structure height is comparable with the bubble departure diameter, bubble nucleation and growth may occur inside the structures [37].

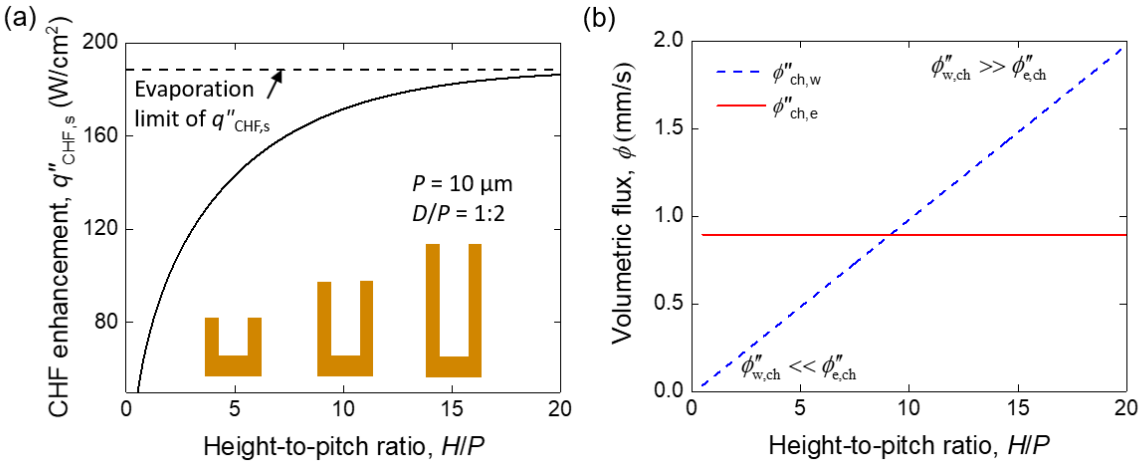

Figure 7. Effect of the height-to-pitch ratio H/P on CHF showing (a) the CHF enhancement $q''_{CHF,s}$ and (b) the characteristic wicking flux $\phi''_{w,ch}$ and characteristic evaporation flux $\phi''_{e,ch}$ as a function of the height-to-pitch ratio H/P for water boiling on square micropillar arrays (P = 10 μm and D/P = 1:2).

Several key design criteria emerge from the parametric study of CHF enhancement on surfaces with square micropillar arrays:

i) For a fixed *D*:*P*:*H* ratio, an optimal structure size exists that maximizes structure-induced CHF enhancement $q''_{\mathrm{CHF,s}}$ based on the competition between wicking and evaporation; $q''_{\mathrm{CHF,s}}$ is limited by wicking at a small structure size, and by evaporation at a large structure size.

ii) An optimal micropillar diameter-to-pitch ratio exists based on the competition between capillary pressure and viscous resistance and the competition between conduction resistance and liquid-vapor interfacial resistance. The wicking flux is limited by capillary pressure at a small micropillar diameter-to-pitch ratio and by viscous resistance at a large diameter-to-pitch ratio. The evaporation flux is limited by the conduction resistance at a small diameter-to-pitch ratio and by the liquid-vapor interfacial resistance at a large diameter-to-pitch ratio.

iii) Increasing micropillar height-to-pitch ratio leads to larger CHF enhancement. This effect plateaus with height-to-pitch ratio, and no significant enhancement is observed at a height-to-pitch ratio above $H/P = 20$.

Although the above analysis is performed based on square micropillar arrays, the general mechanisms revealed by the results – specifically the competition between the various transport mechanisms – can be used to guide the design of other wicking structures. Furthermore, parametric optimization for regular wicking structure geometries can be easily performed with the model developed here, provided that accurate wicking and evaporation characteristics are available.

3.3 Comparison with experimental studies

The predictions from the CHF model developed above are compared with experimental data in the literature for water boiling on square micropillar arrays [2, 3, 7, 11] in Figure 8. The model-predicted CHF is calculated using the micropillar geometry, wettability, and material properties reported in [2, 3, 7, 11], as listed in Section S2 of the Supplementary Material. A roughness factor of $r_{\mathrm{s}} = \pi/2$ is used to account for the roughness on the side wall of the micropillars fabricated with deep reaction ion etching (DRIE) [16]. This comparison includes experimental data for water boiling on various micropillar arrays having different surface coatings, including bare silicon (no coating) [7], silicon oxide [3, 11], and gold [2]. The water contact angle at the boiling point (100

°C at atmospheric pressure) is estimated following Chu *et al.*'s analysis of the effect of temperature on the contact angle [38]. As shown in Figure 8, good general agreement is observed, with all of the experimental data for these different surfaces collapsing to the model prediction line. A much clearer trend is demonstrated between the experimental values of CHF and those predicted from our model based on a balance between wicking and evaporation relative to the mapping of CHF against the wicking rate alone in Figure 2. This demonstrates that the balance between evaporation and wicking in the liquid layer underneath the bubble is a key mechanism that determines the critical heat flux during pool boiling on structured surfaces.

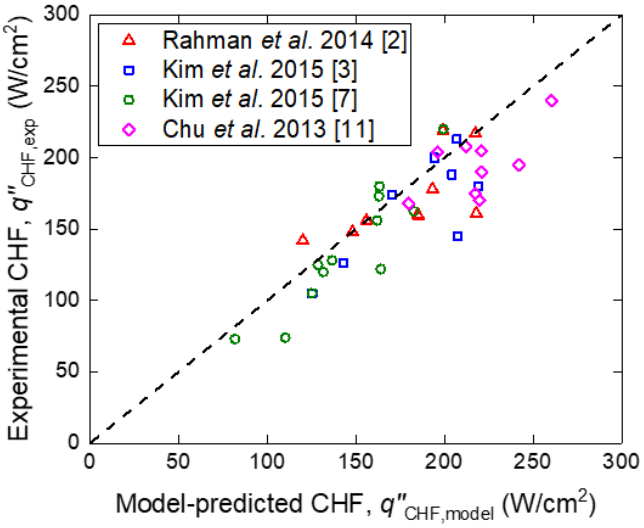

Figure 8. Comparison between the wicking-enhanced CHF model from this work and experimental pooling boiling CHF data, for water on square micropillar arrays.

4. Conclusions

A predictive model that accounts for the competition between wicking and evaporation in the liquid layer underneath the bubbles is developed for the structure-enhanced CHF during boiling on structured surfaces. A dry-spot diameter is calculated by balancing the wicking rate and evaporation rate in the liquid layer underneath the bubble. The structure-induced CHF enhancement is determined based on this dry spot diameter. The model builds on existing CHF models based on wicking alone. In addition, the model also accounts for *radial* wicking behavior underneath the bubble during boiling as well as the nonequilibrium meniscus profile within the micropillar array. The model predictions are shown to agree with experimental CHF data for water

boiling on micropillar arrays with different surface geometry and wettability, demonstrating the expanded generality of the present model compared to existing CHF correlations and models.

A parametric study was performed to investigate the effects of the microstructure geometry on the CHF enhancement for water boiling on square micropillar arrays using the model. Three design criteria were identified for structure optimization to improve boiling critical heat flux. For a fixed *D*:*P*:*H* ratio, an optimal micropillar size is identified at which CHF is maximized based on the competition between wicking and evaporation. An optimal diameter-to-pitch ratio is also identified based on the competition between capillary pressure and viscous resistance, as well as the competition between the conduction resistance and liquid-vapor interfacial resistance. The structure-induced CHF enhancement is found to increase monotonically with the micropillar height-to-pitch ratio due to stronger wicking. However, this increase becomes insignificant for very large height-to-pitch ratio where CHF is limited by evaporation. This model can be used to guide the design of surface structures to enhance critical heat flux.

Acknowledgments

This work was supported in part by Purdue's NEPTUNE Center for Power and Energy, funded by the Office of Naval Research under Grant No. N000141613109. This work used the Extreme Science and Engineering Discovery Environment (XSEDE), which is supported by National Science Foundation grant number ACI-1548562.

Appendix A. Supplementary material

Supplementary data associated with this article can be found in the online version.

References

[1] N. Zuber, Hydrodynamic aspects of boiling heat transfer, PhD Thesis, University of California, Los Angeles, 1959.
[2] M.M. Rahman, E. Ölçeroğlu, M. McCarthy, Role of wickability on the critical heat flux of structured superhydrophilic surfaces, Langmuir, 30 (2014) 11225−11234.
[3] D.E. Kim, D.I. Yu, S.C. Park, H.J. Kwak, H.S. Ahn, Critical heat flux triggering mechanism on micro-structured surfaces: Coalesced bubble departure frequency and liquid furnishing capability, Int. J. Heat Mass Transfer, 91 (2015) 1237-1247.
[4] A.R. Betz, J. Xu, H.H. Qiu, D. Attinger, Do surfaces with mixed hydrophilic and hydrophobic areas enhance pool boiling?, Appl. Phys. Lett., 97 (2010) 141909.

[5] J.A. Weibel, S.V. Garimella, M.T. North, Characterization of evaporation and boiling from sintered powder wicks fed by capillary action, Int. J. Heat Mass Transfer, 53 (2010) 4204-4215.
[6] H.W. Moon, Y.J. Yoon, J.H. Park, B.S. Myung, D.E. Kim, Dynamic wetting and boiling characteristics on micro-structured and micro/nano hierarchically structured surfaces, Exp. Therm Fluid Sci., 74 (2016) 19-26.
[7] S.H. Kim, G.C. Lee, J.Y. Kang, K. Moriyama, M.H. Kim, H.S. Park, Boiling heat transfer and critical heat flux evaluation of the pool boiling on micro structured surface, Int. J. Heat Mass Transfer, 91 (2015) 1140-1147.
[8] D.E. Kim, S.C. Park, D.I. Yu, M.H. Kim, H.S. Ahn, Enhanced critical heat flux by capillary driven liquid flow on the well-designed surface, Appl. Phys. Lett., 107 (2015) 023903.
[9] H. Honda, H. Takamastu, J.J. Wei, Enhanced boiling of FC-72 on silicon chips with micro-pin-fins and submicron-scale roughness, J. Heat Transfer, 124 (2001) 383-390.
[10] N.S. Dhillon, J. Buongiorno, K.K. Varanasi, Critical heat flux maxima during boiling crisis on textured surfaces, Nat. Commun., 6 (2015) 1-12.
[11] K.H. Chu, Y.S. Joung, R. Enright, C.R. Buie, E.N. Wang, Hierarchically structured surfaces for boiling critical heat flux enhancement, Appl. Phys. Lett., 102 (2013) 151602.
[12] A. Zou, D.P. Singh, S.C. Maroo, Early evaporation of microlayer for boiling heat transfer enhancement, Langmuir, 32 (2016) 10808-10814.
[13] H.J. Kwak, J.H. Kim, B.-S. Myung, M.H. Kim, D.E. Kim, Behavior of pool boiling heat transfer and critical heat flux on high aspect-ratio microchannels, Int. J. Therm Sci, 125 (2018) 111-120.
[14] S. Sarangi, J.A. Weibel, S.V. Garimella, Quantitative evaluation of the dependence of pool boiling heat transfer enhancement on sintered-particle coating characteristics, J. Heat Transfer, 139 (2017) 021502.
[15] R. Chen, M.C. Lu, V. Srinivasan, Z. Wang, H.H. Cho, A. Majumdar, Nanowires for Enhanced Boiling Heat Transfer, Nano Lett., 9 (2009) 548-553.
[16] K.H. Chu, R. Enright, E.N. Wang, Structured surfaces for enhanced pool boiling heat transfer, Appl. Phys. Lett., 100 (2012) 241603.
[17] H.S. Ahn, G. Park, J.M. Kim, J. Kim, M.H. Kim, The effect of water absorption on critical heat flux enhancement during pool boiling, Exp. Therm Fluid Sci., 42 (2012) 187-195.
[18] S. Bhavnani, V. Narayanan, W. Qu, M. Jensen, S. Kandlikar, J. Kim, J. Thome, Boiling Augmentation with Micro/Nanostructured Surfaces: Current Status and Research Outlook, Nanosc Microsc Therm, 18(3) (2014) 197-222.
[19] S.G. Kandlikar, Controlling bubble motion over heated surface through evaporation momentum force to enhance pool boiling heat transfer, Appl. Phys. Lett., 102 (2013) 051611.
[20] B.S. Kim, H. Lee, S. Shin, G. Choi, H.H. Cho, Interfacial wicking dynamics and its impact on critical heat flux of boiling heat transfer, Appl. Phys. Lett., 105 (2014) 191601.
[21] R. Li, Z. Huang, A new CHF model for enhanced pool boiling heat transfer on surfaces with micro-scale roughness, Int. J. Heat Mass Transfer, 109 (2017) 1084-1093.
[22] S.G. Kandlikar, A theoretical model to predict pool boiling CHF incorporating effects of contact angle and orientation, J. Heat Transfer, 123 (2001) 1071-1079.
[23] R. Xiao, R. Enright, E.N. Wang, Prediction and optimization of liquid propagation in micropillar arrays, Langmuir, 26 (2010) 15070-15075.
[24] T.P. Allred, J.A. Weibel, S.V. Garimella, A wettability netric for characterization of capillary flow on textured superhydrophilic surfaces, Langmuir, 33 (2017) 7847-7853.

[25] V.K. Dhir, S.P. Liaw, Framework for a unified model for nucleate and transition pool. Basicaly your J. Heat Transfer, 111 (1989) 739-746.
[26] D. Quéré, Wetting and roughness, Annu. Rev. Mater., 38 (2008) 71-99.
[27] H. Brinkman, A calculation of the viscous force exerted by a flowing fluid on a dense swarm of particles, Appl. Sci. Res., 1 (1949) 27-34.
[28] W. Fritz, Maximum volume of vapor bubbles, Phys. Zeitschrift, 36 (1935) 379.
[29] Y. Nam, E. Aktinol, V.K. Dhir, S. Ju, Single bubble dynamics on a superhydrophilic surface with artificial nucleation sites, Int. J. Heat Mass Transfer, 54 (2011) 1572-1577.
[30] L. Dong, X. Quan, P. Cheng, An experimental investigation of enhanced pool boiling heat transfer from surfaces with micro/nano-structures, Int. J. Heat Mass Transfer, 71 (2014) 189-196.
[31] A. Tamayol, M. Bahrami, Analytical determination of viscous permeability of fibrous porous media, Int. J. Heat Mass Transfer, 52 (2009) 2407-2414.
[32] K. Yazdchi, S. Srivastava, S. Luding, Microstructural effects on the permeability of periodic fibrous porous media, Int. J. Multiphase Flow, 37 (2011) 956-966.
[33] S. Cho, R. Tummala, Y. Joshi, Capillary performance of micropillar arrays in different arrangements, Nanosc Microsc Therm, 22 (2018) 97-113.
[34] H. Wang, S.V. Garimella, J.Y. Murthy, Characteristics of an evaporating thin film in a microchannel, Int. J. Heat Mass Transfer, 50 (2007) 3933-3942.
[35] B. Paul, Compilation of evaporation coefficients, ARS Journal, 32 (1962) 1321-1328.
[36] S. Adera, D. Antao, R. Raj, E.N. Wang, Design of micropillar wicks for thin-film evaporation, Int. J. Heat Mass Transfer, 101 (2016) 280-294.
[37] S. Sarangi, J.A. Weibel, S.V. Garimella, Effect of particle size on surface-coating enhancement of pool boiling heat transfer, Int. J. Heat Mass Transfer, 81 (2015) 103-113.
[38] K.-H. Chu, R. Enright, E.N. Wang, Microstructured surfaces for enhanced pool boiling heat transfer, Proceedings of the ASME 2011 International Mechanical Engineering Congress and Exposition, Denver, Calarodo, November 11-17 (2011) IMECE2011-65169.